Temperature Dependence of the Kerr Nonlinearity and Two-Photon Absorption in a Silicon Waveguide at 1.55 μm

Gary F. Sinclair,* Nicola A. Tyler, Döndü Sahin, Jorge Barreto, and Mark G. Thompson
Quantum Engineering Technology Labs, School of Physics, H.H. Wills Physics Laboratory, University of Bristol, Tyndall Avenue, Bristol BS8 1TL, United Kingdom

(Received 11 September 2018; revised manuscript received 19 February 2019; published 25 April 2019)

We measure the temperature dependence of the two-photon absorption and optical Kerr nonlinearity of a silicon waveguide over a range of temperatures from 5.5 to 300 K. Measurements are taken at a wavelength of 1.55 μm in the technologically important telecom C band. We observe a near halving (45% reduction) of the two-photon absorption coefficient at low temperature, whereas a smaller reduction in the Kerr nonlinearity of 25% is found. The increased ratio of Kerr to absorptive nonlinearity at low temperatures indicates an improved operation of integrated photonic devices that make use of a nonlinear phase shift, such as optical switches or parametric photon-pair sources. As an example, we examine how the heralding efficiency of a photon-pair source will change at low temperatures and predict a modest improvement in source performance. In addition, the modeling and experimental techniques developed can readily be extended to other wavelengths or materials of interest.

DOI: 10.1103/PhysRevApplied.11.044084

I. INTRODUCTION

The high effective nonlinearity and mature fabrication technology offered by silicon photonics presents a useful platform for constructing integrated nonlinear photonic devices. A variety of applications have been demonstrated that make use of the high Kerr nonlinearity present in silicon, including optical frequency combs [1], all-optical switching [2] and logic [3], parametric amplification for frequency conversion [4,5], and parametric photon-pair sources [6,7] for quantum-information processing. Often, the presence of two-photon absorption and subsequent free-carrier effects act as a parasitic mechanism in these devices, although these effects have been put to positive use in all-optical logic [8] and adiabatic frequency conversion [9]. Driven by these applications, there has been a considerable effort to accurately measure [10–12] and model [13–15] the nonlinear optical properties of silicon. Although these studies have focused on room-temperature measurements, some investigations of the temperature dependence of the one- and two-photon indirect absorption coefficient at a wavelength of 1.06 μm [16,17] and free-carrier lifetime [18] have been performed. At this wavelength, a strong temperature dependence of the one-photon indirect absorption coefficient has been observed, showing a two-orders-of-magnitude change over the 100- to 300-K range [17]. However, no study of the temperature dependence of the Kerr nonlinearity and two-photon absorption has been performed at wavelengths around 1.55 μm in the telecom C band, as commonly used in most integrated silicon-photonic devices.

One application area that is likely to require cryogenic operation is integrated quantum photonics. Waveguide-integrated single-photon detectors are essential for measurement-based quantum computing [19]. To achieve high-efficiency, low-noise detection along with fast control feedback, the monolithic integration of superconducting nanowire single-photon detectors with photonic circuits is required [20,21]. Operation of the chip at few-Kelvin temperatures potentially impacts the performance of nonlinear photonic components, such as parametric photon-pair sources, where the brightness, purity, and heralding efficiency depend on the nonlinear optical parameters of the waveguide [22,23]. In particular, the heralding efficiency of a photon-pair source is known to be adversely affected by the nonlinear cross two-photon absorption present in silicon at wavelengths in the telecom C band [23]. Furthermore, although the spontaneous Raman scattering peak of pump photons occurs at 15.6 THz away from the pump [24], a low-power broad-band inelastic scattering has also been observed close to the pump wavelength [25]. This result suggests a further motivation for the operation of sources at cryogenic temperatures, where the effect of this noise on source performance will be reduced. Additionally, silicon photonics also offers a promising platform for chemical and biological sensing in the mid-infrared wavelength range where the fundamental vibrational modes of most chemical bonds are present [26,27].

*gary.f.sinclair@bristol.ac.uk

However, at longer wavelengths, background thermal noise becomes an ever larger constraint on device performance [26,28], suggesting that low-temperature operation could be of benefit.

In this article, we determine the Kerr nonlinearity and two-photon absorption (TPA) present in a silicon waveguide between the temperatures of 5.5 and 300 K at a wavelength of 1.55 μm. By modeling the propagation of a short optical pulse along a waveguide, we can relate the observed nonlinear transmission and pulse spectral broadening to the nonlinear waveguide parameters. This is the first measurement of both the TPA and Kerr nonlinearity at cryogenic temperatures in the technologically important telecom C band. In addition, although the techniques developed have been used to characterize a silicon waveguide at 1.55 μm, they could more generally be applied to other third-order nonlinear materials and at other wavelengths.

II. MODELING PULSE PROPAGATION

We begin by constructing a model of pulse propagation through a nonlinear optical waveguide. The propagation of an optical pulse is commonly described by the nonlinear Schrödinger equation [29],

$$\frac{\partial E}{\partial z} = \left(ik_o n_2 - \frac{\beta_{\mathrm{TPA}}}{2}\right)|E|^2 E - \frac{\sigma_{\mathrm{FCA}}}{2}(1+i\mu)N_c E - \frac{\alpha}{2}E, \tag{1}$$

where E is the electric field envelope (in units of $\sqrt{\mathrm{W/m^2}}$), $k_o = 2\pi/\lambda$ is the wave number, n_2 is the Kerr coefficient, β_{TPA} is the TPA coefficient, σ_{FCA} is the free-carrier absorption (FCA) coefficient, μ determines the relative strength of the free-carrier dispersion (FCD), N_c is the free-carrier density, and α is the linear loss. The generation of free carriers at each point of the waveguide is governed by

$$\frac{\partial N_c}{\partial t} = \frac{\beta_{\mathrm{TPA}}}{2\hbar\omega}|E|^4 - \frac{N_c}{t_c}, \tag{2}$$

where t_c is the free-carrier lifetime. An exact closed-form solution of these propagation equations can be found when free-carrier effects can be neglected, as occurs when the pulse energy and repetition rate are sufficiently low [29]. Alternatively, an approximate solution can also be found when free-carrier effects only weakly modify the pulse shape [30]. In our work, we do not make either of these approximations and choose to numerically solve the propagation equations, as detailed in Appendix A. Briefly, the propagation equations are solved using a first-order finite-difference method [31], assuming excitation of the quasi-transverse-electric (quasi-TE) mode of a 220 × 500-nm silicon-on-insulator waveguide of length 19.09 mm. Figure 1 shows (a) the output pulse power and (b) the phase, as predicted by our model for room-temperature values of the nonlinear parameters and a high-power input pulse (5-mW in-waveguide power). At this power, the short duration (4.9 ps) and low repetition rate of our optical pulses ensures that TPA makes the largest contribution to the nonlinear loss. However, the effect of free carriers is equally as important as the Kerr nonlinearity for the phase. As can be seen from Fig. 1(b), self-phase modulation (SPM) and TPA result in a nonlinear phase profile that approximately reflects the input pulse shape. However, the addition of free-carrier effects into the model results in a reduction of the peak nonlinear phase due to FCA and an asymmetry in the phase profile due to FCD. The asymmetry arises due to the accumulation of free carriers over the pulse duration. We note that FCD and the Kerr nonlinearity act with opposite signs on the pulse phase. Free-carrier effects are included in the model, using a temperature-dependent model for the FCA parameter (see Appendix A).

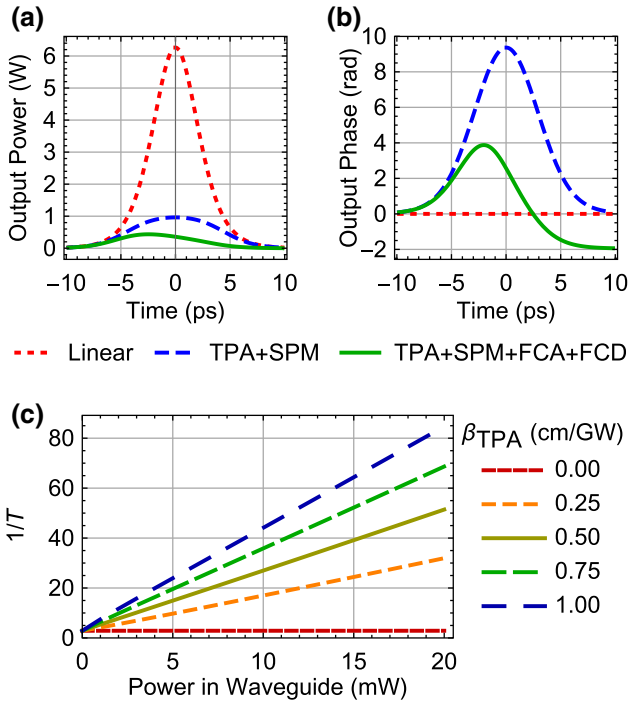

FIG. 1. (a) The modeled output power and (b) phase of a 4.9-ps pulse with peak in-waveguide power of 18.0 W (5 mW average) and room-temperature nonlinear parameter values. (c) The modeled inverse transmission of a pulse for a range of two-photon absorption parameters and fixed room-temperature FCA, as a function of the time-averaged input power at the start of the waveguide.

Following earlier works [16,17,32], we monitor the inverse transmission through the waveguide ($1/T = P_{\mathrm{in}}/P_{\mathrm{out}}$), where the time-averaged power is $P = \Gamma \int_{\mathrm{pulse}} P(\tau)d\tau$, Γ is the laser repetition rate, and the time integral is taken over the input or output pulse as

appropriate. Plotting of the inverse transmission is chosen, rather than the transmission, as this more effectively decouples the fitting parameters (linear loss and TPA parameter), as discussed below. Figure 1(c) shows the modeled inverse transmission along the waveguide (not including coupling losses) for a range of TPA coefficients (β_{TPA}) and a fixed room-temperature value for FCA (see Appendix A). When $\beta_{TPA} = 0$, there is no nonlinear absorption and the inverse transmission is a constant, equal to the inverse of the linear propagation loss along the waveguide (2.4 dB/cm). The inverse transmission is seen to remain almost as a straight line with an increasing slope for larger values of the TPA parameter. Plotting the data in this way has the benefit of decoupling the two fit parameters: the intercept, from which the linear loss is deduced, and the slope, from which the TPA parameter is found. This method leads to more accurate fits when analyzing noisy data.

III. EXPERIMENTAL SETUP

Figure 2 depicts the setup used to take measurements of the transmission and spectrum of an optical pulse after propagation through the waveguide at various temperatures between 5.5 and 300 K. Optical pulses of 4.9-ps full-width half-maximum (FWHM) are generated by a PriTel Femtosecond Fiber Laser, with a repetition rate of 50 MHz, 196-W peak power, and wavelength of 1551.8 nm. The pulse duration is measured using an intensity autocorrelator (Femtochrome Research FR-103PD), assuming a sech^2 profile, as expected for a passively mode-locked fiber laser [33]. A variable optical attenuator (Oz Optics, DA-100) is used to step the power linearly between 30 and 0 dB of attenuation. At each attenuation setting (20 in total), the optical spectrum and transmission are recorded (Anritsu MS9740A and Thorlabs S154C power meter respectively). From the transmitted power, the TPA coefficient can be found and, from the recorded transmission spectra, the Kerr nonlinearity can be determined. Before each power scan, the transmission is maximized using a polarization controller (Agilent 11896A) to ensure a consistent polarization state (quasi-TE) in the waveguide. Power is monitored at the input using a 99:1 fiber coupler and at the output using a 50:50 splitter to divide the light equally between the output power meter and optical spectrum analyzer. The splitting ratio and insertion loss of each coupler are measured to ensure that correct estimates of the input/output power can be made. Before coupling light on/off the chip a 2×2 cross-over switch is used to allow light to be propagated in either direction along the waveguide. Any asymmetry in the efficiency of the on-chip grating couplers can be compensated for by taking measurements in both orientations, as discussed in Appendix B. At each temperature setting, transmission and spectral measurements are taken in pairs at each power setting: initially with the light propagating along the waveguide in one direction and then in the reverse direction. Multiple pairs of measurements are taken for each temperature setting to monitor the reproducibility of our data.

The device under test consists of a 19.09-mm channel waveguide with a cross section of 220×500 nm and is fabricated by the Institute of Microelectronics through a multiproject wafer service (full details of the platform can be found in Ref. [34]). The chip is cooled in a Lakeshore Cryogenic Probe Test Station (Model CPX), which is modified to allow vertical coupling to and from the chip via focused grating couplers (approximately 5-dB loss per coupler). Coupling to the chip is via a V-groove fiber array and is optimized during the experiment by manual adjustment of the fiber position and angle using a five-axis control stage. The cryostat allows cooling of the chip to a minimum of 5.5 K, maintaining a temperature stability of at least 0.1 K. Between each temperature setting, the system is typically allowed 15 min to reach thermal equilibrium and steady coupling.

IV. RESULTS

A. Two-photon absorption

Using the model developed above, the inverse transmission data [35] for each power scan are fitted to extract the

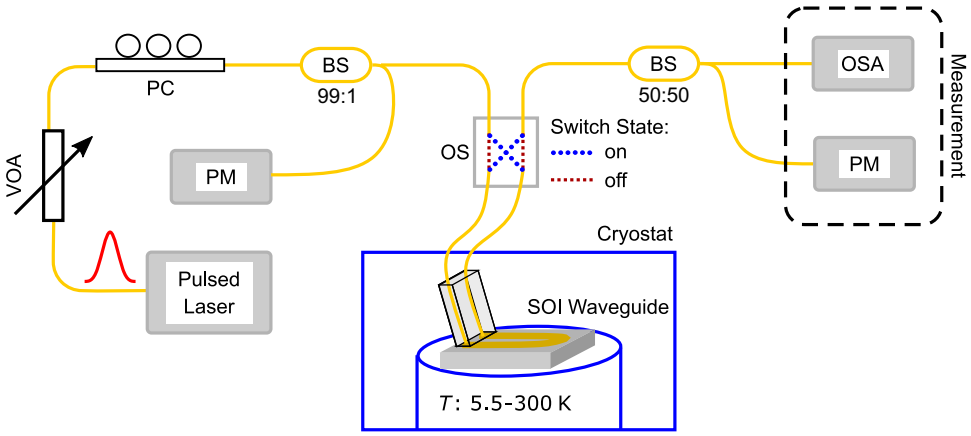

FIG. 2. The experimental setup used when measuring the transmission and spectral broadening of pulses transmitted through a silicon waveguide: VOA, variable optical attenuator; SMF, single-mode fiber; PC, polarization controller; BS, fiber beam splitter; OS, 2×2 optical cross-over switch; OSA, optical spectrum analyzer; PM, power meter; SOI, silicon-on-insulator.

TPA coefficient. Figure 3 shows example fits at 5.5 and 300 K. The transmission shown in the figure is measured across the optical switch and, therefore, includes losses due to the optical switch, grating couplers, and waveguide. Because of the asymmetry of the grating couplers, a larger apparent nonlinearity is observed in the off direction, as indicated by the larger gradient of the fit. This result occurs because, given the same overall linear loss, if the input grating coupler has a lower loss than the output, then the larger power in the waveguide gives rise to a larger nonlinear response. By taking data in both orientations, the correct TPA coefficient can be found from the geometric mean of the pair (see Appendix B). We note that the cross-over switch introduces a slight excess loss when in the on state, as indicated by the larger value of $1/T$ at the zero-power intercept, althoughthis loss does not affect the fitted TPA value. Data at low temperatures suffer from greater noise due to fluctuations in the coupling caused by a mechanical resonance of the cryostat sample stage. This noise is particularly noticable at temperatures below 50 K. To compensate for the noise, a larger number of power scans are taken at lower temperatures than at higher ones (at least 20 scans at each temperature below 50 K and at least 6 scans at each temperature above 50 K). In total, 432 pairs of power scans are taken across the entire temperature range.

Figure 4(a) shows the fitted TPA coefficient extracted from the inverse transmission power scans. Each point in the graph is the arithmetic mean of the TPA coefficient determined from several pairs of transmission measurements taken in both directions, where the error bars are the standard deviation of the individual pairwise measurements. We fit our data by following Ref. [14] and assuming that the dominant contribution to the TPA comes from phonon-assisted two-photon allowed-allowed transitions across the lowest indirect band gap. In addition, we include contributions from both transverse acoustic ($E_{\rm ph}^{\rm TA}/k_B =$ 212 K) and transverse optical ($E_{\rm ph}^{\rm TO}/k_B = 670$ K) phonon branches as follows [36]:

$$\beta_{\rm TPA} = E_{\rm gap}(T)^{3/2} \sum_b \{K_b[F_+^b(T) + F_-^b(T)]\}. \quad (3)$$

Here, $b \in \{\rm TA, TO\}$ sums over the phonon branches and $F_\pm^b$ arise due to terms involving the creation (+) or annihilation (−) of a phonon in the corresponding branch as follows:

$$F_+^b(T) = \frac{(2\hbar\omega - E_{\rm gap}(T) - E_{\rm ph}^b)^2}{\exp[E_{\rm ph}^b/(k_B T)] - 1}, \quad (4)$$

$$F_-^b(T) = \frac{(2\hbar\omega - E_{\rm gap}(T) + E_{\rm ph}^b)^2}{1 - \exp[-E_{\rm ph}^b/(k_B T)]}, \quad (5)$$

where $\hbar\omega$ is the photon energy (0.797 eV) and $E_{\rm gap}(T) = E_{\rm gap}(0) - \beta T^2/(T+\delta)$ is the temperature-dependent band gap, where the values $E_{\rm gap}(0) = 1.156$ eV, $\beta = 7.021 \times 10^{-4}$ eV K^{-1}, and $\delta = 1108$ K are taken from Ref. [37]. As is apparent from Fig. 4(a), the temperature dependence of the TPA is well represented by Eq. (3), where we find the fit parameters $K_{\rm TA} = 0.233$ and $K_{\rm TO} = 2.138$. We note that the largest contribution to the temperature dependence (approximately 80%) comes from the phonon population, rather than the change in the band gap. This contribution is estimated by using Eq. (3), with the fit parameters found, to compare the change in TPA with and without a temperature-dependent band gap. Since the two-photon transition is phonon assisted, the transition probability is seen to decrease at lower temperatures as the phonon

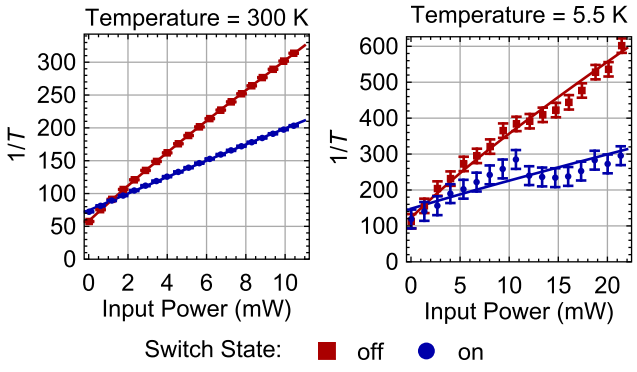

FIG. 3. Model fits to the measured inverse transmission (fiber to fiber) at temperatures of 300 and 5.5 K. Data are taken with light propagating in both directions along the waveguide, as indicated by the cross-over switch being in the on or off state.

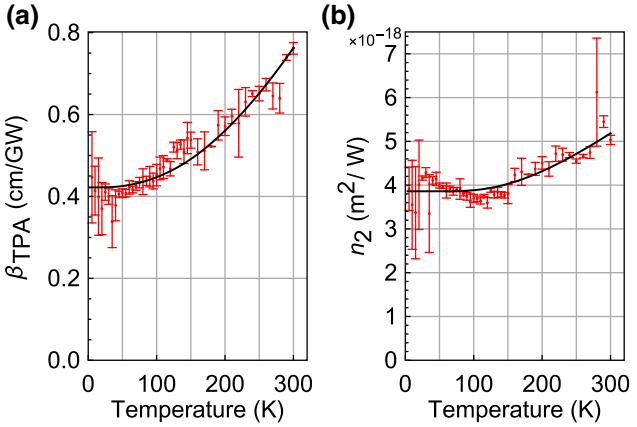

FIG. 4. (a) The two-photon absorption as a function of temperature, fitted using Eq. (3). Based on the fitting, TPA is seen to decrease by 45% from 300 to 5.5 K. (b) The Kerr nonlinearity, fitted using Eq. (6). A smaller reduction in the Kerr nonlinearity of 25% is observed over the same temperature range.

population declines. However, transitions are always possible even in the absence of a significant thermal bath of phonons, as a phonon can be created to assist the transition. In addition, since the energy of two photons (approximately 1.6 eV) is significantly larger than the band gap (1.12 to 1.16 eV), we do not expect small changes in the band gap to significantly change the density of states [38]. This result is in contrast to one-photon indirect transitions at 1.06 μm, where the rapidly changing density of states close to the band edge leads to a much larger temperature dependence of the absorption [17].

In addition to using the transmission data to calculate the TPA coefficient, it is also possible to determine the individual coupling losses of the grating couplers. This result is deduced from the asymmetry of the apparent TPA value measured in each direction using Eq. (B6). By determining the individual coupling losses in this way, the in-waveguide power for each measurement is determined, thereby removing this uncertainty in subsequent analysis.

B. Kerr nonlinearity

To determine the Kerr nonlinearity, the output spectrum of the transmitted pulse is measured at a range of input powers, as shown in Fig. 5(a). As expected, SPM causes a broadening of the pulse spectrum as the input power is increased. A very slight blueshift of the central wavelength can also be seen due to FCD. For each input power, the temporal phase of the output pulse is reconstructed using the Gerchberg-Saxton phase retrieval algorithm, full details of which can be found in Ref. [39]. This algorithm requires knowledge of the output power spectrum, which is straightforward to measure using an optical spectrum analyzer, and the pulse envelope in the time domain. To estimate the pulse shape at the output of the waveguide, we use the transmission data (discussed above) to determine the degree to which the pulse is distorted due to the nonlinear absorption from the initial pulse profile. This estimated output pulse shape is used in the algorithm to reconstruct the pulse phase. We note, however, that the reconstructed phases are quite insensitive to the exact shape of the temporal pulse envelope, as the observed spectral broadening is largely due to the nonlinear phase imparted to the pulse, rather than the distortion of the pulse envelope [29].

A selection of reconstructed phase profiles and fits to our numerical pulse evolution model is shown in Fig. 5(b). All reconstructed phases are baseline corrected against the lowest power (0.02 mW) scan, which is why this figure appears as a flat phase profile. Although the input pulse is not, in fact, transform limited, the additive nature of the accumulated phase means that the exact input phase profile is not important, so long as the temporal pulse length is correctly known. In addition, because of the significant length of optical fiber in our setup, it is necessary to subtract the background phase accumulated due to SPM in the

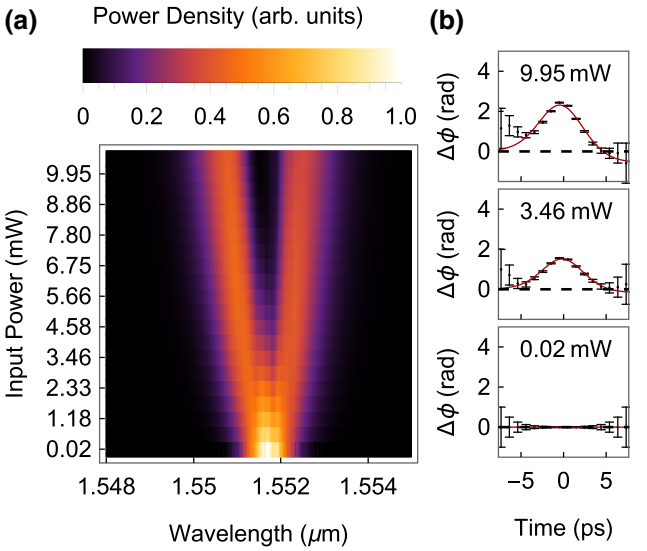

FIG. 5. (a) The measured power spectrum at the output of the waveguide. Each power spectrum (horizontal cross section of the plot) is normalized to the same total pulse energy for clarity. (b) The reconstructed temporal phase ($\Delta\phi$) of the output pulse for three different input powers: black points denote data and the red line shows the fitted numerical model.

optical fibers. Removing this background contribution to the nonlinear phase is necessary; otherwise, this process would lead to an overestimate of the Kerr nonlinearity in the waveguide. To characterize the background Kerr nonlinearity, a series of transmission spectra through the chip are measured as the coupling to the chip is gradually decreased. The spectral broadening is seen to decrease as the power in the waveguide drops. Once the fiber-to-fiber excess loss is increased to approximately 20 dB, the output spectrum is seen to remain constant as the chip is further decoupled. This result indicates that pulse propagation in the chip is of sufficiently low power so as to be in the linear regime, whereas the nonlinearity produced in the fibers leading up to the chip can still be measured. A power scan is taken at this decoupling to characterize the Kerr nonlinearity of the input fibers, allowing us to subtract this background contribution to the phase from all of our subsequent measurements when the chip is well coupled. No significant further nonlinearity is expected in the output fibers, due to the lower power present after the chip. The reconstructed phases shown in Fig. 5(b) are background corrected using the method described. As can be seen, the reconstructed phases clearly exhibit a profile consistent with SPM due to the Kerr nonlinearity. We use the numerical model developed to fit the phase profiles and extract the Kerr nonlinearity for each of the reconstructed phase profiles, as discussed in Appendix B. During this fitting, the in-waveguide power determined when fitting the transmission data is used, removing the need to compensate for the

asymmetric coupling losses by taking the geometric mean of pairs of measurements in each direction.

Figure 4(b) shows the measured Kerr coefficient as a function of the sample temperature. Although some temperature dependence is observed, the decrease in Kerr nonlinearity at low temperatures (25%) is seen to be a little over half of the decline (45%) observed in the absorptive nonlinearity. We choose to fit the data to an empirical model motivated by that used for the TPA coefficient as follows:

$$n_2(T) = n_2(0)\left[\frac{1}{\exp(E_{\mathrm{ph}}/k_B T)-1} + \frac{1}{1-\exp(-E_{\mathrm{ph}}/k_B T)}\right]. \tag{6}$$

Here, the fit parameters are the Kerr coefficient at 0 K, $n_2(0) = 3.86 \times^{-18}$ m^2 W^{-1}, and a parameter $E_{\mathrm{ph}}/k_b = 576$ K, which has the form of the phonon energy and is somewhat close to the value of the transverse optical phonon energy. We stress that this model is purely empirical and is chosen to match the data in the absence of any other known models for the predicted temperature dependence of the Kerr nonlinearity.

V. NONLINEAR FIGURE OF MERIT

In many photonic applications, TPA acts as a parasitic nonlinear loss mechanism, reducing the amount of useful Kerr nonlinearity that can be achieved. For instance, it has been shown that TPA places a limit on the losses of an all-optical switch [40] and that this loss can be further compounded at high switching rates by subsequent free-carrier effects [2]. Similarly, it has been proposed that cross two-photon absorption (XTPA) between pump and signal/idler photons in a parametric photon-pair source acts as a fundamental limit to the heralding efficiency of such sources [23]. For these applications, it can be useful to introduce the dimensionless figure of merit FOM $= n_2/(\lambda\beta_{\mathrm{TPA}})$ to describe the ratio of the useful Kerr nonlinearity to the parasitic TPA [40,41]. Here, we briefly investigate how the heralding efficiency of a parametric photon-pair source can be understood to depend on the nonlinear FOM.

As an illustration, we consider the simplest possible photon-pair source: a single-mode, nondispersive, silicon waveguide. For this type of source, photon pairs are generated over a broad bandwidth and narrow-band filtering is applied to the herald photon to improve the purity of the heralded photons. It has been shown that the probability of generating one photon pair per pulse can be written as [22]

$$p_{\mathrm{pair}} = \frac{(\gamma L P)^2}{2}\sqrt{\frac{1-\mathcal{P}^2}{\mathcal{P}}}, \tag{7}$$

where $\gamma = (k_0 n_2)/A_{\mathrm{eff}}$ is the waveguide nonlinear parameter, A_{eff} is the effective area of the waveguide, P is the pump peak power, L is the waveguide length, and $\mathcal{P}$ is the purity of the heralded photons. Here, the source is assumed to be operating in the weakly pumped regime, so that higher-order terms can be neglected. If the only loss mechanism present is XTPA, then the heralding efficiency (also known as the Klyshko efficiency [42,43]) is limited only by the probability of XTPA between the pump and heralded photons [23]. Therefore, the heralding efficiency is equal to

$$\eta_{\mathrm{heralding}} = \frac{1}{(1+\xi)^2}, \tag{8}$$

where $\xi = \alpha_{\mathrm{TPA}} L P$ is a dimensionless parameter describing the nonlinear loss and $\alpha_{\mathrm{TPA}} = \beta_{\mathrm{TPA}}/A_{\mathrm{eff}}$ is the waveguide nonlinear absorption parameter. Using Eq. (7) and the definition of the nonlinear FOM, we find that we can express ξ in terms of the source purity, brightness, and material FOM:

$$\xi = \frac{1}{2\pi\,\mathrm{FOM}}\sqrt{2 p_{\mathrm{pair}}\frac{\mathcal{P}}{\sqrt{1-\mathcal{P}}}}. \tag{9}$$

Evaluating the heralding efficiency for some reasonable parameters ($p_{\mathrm{pair}} = 0.05, \mathcal{P} = 0.9$), we find a room-temperature heralding efficiency of 0.74, improving to 0.79 at 0 K using FOMs of 0.44 and 0.59 respectively (based on values given in Table I of Appendix A). Thus, cryogenic cooling to 0 K is seen to have a moderately positive effect on heralding efficiency. We note that the nonlinear FOM has been seen to improve significantly at longer wavelengths toward the mid-infrared. This result has led to suggestions to develop integrated silicon photonic components at longer wavelengths. For instance, a room-temperature nonlinear FOM of 4.4 has been measured at 2.2 μm in Ref. [41]. Using this value for the FOM, a heralding efficiency of 0.97 is achieved, demonstrating the importance of the FOM for determining parametric source performance. Nonetheless, we note that this simple source design is not optimized for heralding efficiency, and other designs may exhibit bettern performance without the need to operate at longer wavelengths.

TABLE I. Temperature dependence of the nonlinear parameters.

T (K)	α_{TPA} (cm GW^{-1})	n_2 (mm^2 W^{-1})	σ_{FCA} (10^{-22} m^2)
300	0.761	5.18	3.7
150	0.492	4.03	3.1
50	0.424	3.86	2.7
5.5	0.420	3.86	0.9
0.0	0.420	3.86	0.0

VI. CONCLUSIONS

We measure the temperature dependence of the TPA and Kerr nonlinearity at a wavelength of 1.55 μm in the technologically important telecom C band. TPA is found to decrease by 45% from 300 to 5.5 K, whereas a smaller reduction of 25% is observed for the Kerr nonlinearity. The near halving in TPA contrasts with the near vanishing of the one-photon indirect absorption previously observed at 1.06 μm [17,44]. The significantly stronger temperature dependence at the shorter wavelength is believed to be due to the very rapidly changing density of states close to the band edge, whereas at 1.55 μm, the reduction in absorption is primarily due to the reduction in phonon population.

The stronger reduction in TPA as compared to Kerr nonlinearity leads to an improved nonlinear figure of merit at low temperatures. We discuss how the nonlinear FOM is an important metric that determines the performance of many nonlinear photonic devices, such as all-optical switches and parametric photon-pair sources. In particular, we examine how the heralding efficiency of a simple waveguide parametric photon-pair source depends on the nonlinear FOM and show a moderate improvement in heralding efficiency at low temperatures.

When characterizing the nonlinearity of our silicon waveguide, several techniques are employed that may be applicable to other nonlinear integrated photonic experiments. In particular, the use of bidirectional measurements to eliminate coupling-loss uncertainty and phase retrieval of the measured spectra to visualize the time-domain nonlinear effects may be of general use to the community.

ACKNOWLEDGMENTS

This work is supported by the Engineering and Physical Sciences Research Council (EPSRC) under Grant No. EP/L024020/1. M.G.T. acknowledges fellowship support from EPSRC Grant No. EP/K033085/1. The authors would also like to thank Gerardo E. Villarreal-Garcia and Antonio A. Gentile for assistance with cryogenic equipment.

APPENDIX A: MODELING PULSE PROPAGATION

A comprehensive account of modeling nonlinear optical phenomena in silicon waveguides is provided in Ref. [45]. However, some of the more immediately relevant fundamentals from that paper are outlined below for convenience. Equation (1) describes the propagation of an optical pulse, where the electric field $E = E(\vec{r}, \tau)$; $\vec{r}$ is the position vector; $\tau = t - z/v_g$ is the retarded time (where propagation is along the z-axis and v_g is the group velocity); and the electric field is measured in units of $\sqrt{\mathrm{W/m^2}}$. It is convenient to factorize the electric field such that $E = F(x,y)A(z,\tau)$, where $F(x,y)$ is the dimensionless transverse mode profile ($F \in [0,1]$) and $A(z,\tau)$ describes evolution along the propagation axis. However, in most waveguide experiments it is the optical power, rather than the intensity, that is measured. We therefore choose to introduce $\bar{A}(z,\tau) = [\int |F(x,y)|^2 dxdy]^{1/2} A(z,\tau)$, where $\bar{A}$ has units of $\sqrt{\mathrm{W}}$ and $|\bar{A}|^2$ corresponds to the power integrated over the entire mode cross section. Doing so, we find the propagation equation,

$$\frac{\partial \bar{A}}{\partial z} = \left(i\gamma - \frac{\alpha_{\mathrm{TPA}}}{2}\right)|\bar{A}|^2\bar{A} - \frac{\sigma_{\mathrm{FCA}}}{2}(1+i\mu)\bar{N}_c\bar{A} - \frac{\alpha}{2}\bar{A}, \tag{A1}$$

where $\gamma = (k_0 n_2)/A_{\mathrm{eff}}$ and $\alpha_{\mathrm{TPA}} = \beta_{\mathrm{TPA}}/A_{\mathrm{eff}}$ are the nonlinear parameters for the waveguide, $A_{\mathrm{eff}} = [\int |F(x,y)|^2 dx\,dy]^2 / \int_{\mathrm{core}} |F(x,y)|^4 dxdy$ is the effective mode area for SPM (where the lower integral is taken over the nonlinear core only), and other quantities are as defined in Eq. (1). The free-carrier density again has units of m^{-3} but is averaged over the mode cross section as follows:

$$\bar{N}_c(z,t) = \frac{\int N_c(x,y,z,\tau)|F(x,y)|^2 dxdy}{\int |F(x,y)|^2 dxdy}. \tag{A2}$$

By doing so, free carriers are appropriately weighted according to their spatial overlap with the transverse mode in the waveguide. The free-carrier generation equation becomes

$$\frac{\partial \bar{N}_c}{\partial t} = \frac{\bar{\beta}_{\mathrm{TPA}}}{2\hbar\omega}|\bar{A}|^4 - \frac{\bar{N}}{\tau_c}, \tag{A3}$$

and $\bar{\beta}_{\mathrm{TPA}} = \beta_{\mathrm{TPA}} \int_{\mathrm{core}} |F(x,y)|^6 dxdy / \left[\int |F(x,y)|^2 dxdy\right]^3$ is weighted to take account of the mode distribution during the generation process and the subsequent interaction with the field [see Eq. (36) in Ref. [45]]. The transverse mode profile (fundamental quasi-TE mode) is found using a commercial mode solver (Lumerical Mode Solutions). The system of coupled differential equations (A1) and (A3) can now be solved as one-dimensional propagation equations, where all details of the transverse modal structure are absorbed into the definition of the parameters γ and $\bar{\beta}_t extrm TPA$. However, a further simplification can be made by noting that rather than calculating the complex field amplitude, the phase can be calculated from the solution for the power and free-carrier distribution. That is, if we take $\bar{A}(z,\tau) = \sqrt{P(z,\tau)}\exp[i\phi(z,\tau)]$, then from Eq. (A1) we find

$$\frac{\partial P}{\partial z} = -\alpha_{\mathrm{TPA}}P^2 - \sigma_{\mathrm{FCA}}\bar{N}_c P - \alpha P \tag{A4}$$

and the phase of the pulse at the output of the waveguide can be calculated from

$$\phi(L,\tau) = \gamma \int_0^L P(z,\tau)dz - \frac{\sigma_{\mathrm{FCA}}\mu}{2}\int_0^L \bar{N}_c(z,\tau)dz. \tag{A5}$$

Therefore, it is only necessary to numerically calculate the pulse power and free-carrier distribution as a function of position and time, for the range of α_{TPA} and σ_{FCA} values expected and input powers used. This method is in contrast to solving Eq. (A1) directly, which would require numerical solutions for the full range of Kerr and FCD parameters also. Thus, when fitting the reconstructed phases [see Fig. 5(b)], the following much simpler semianalytic phase ansatz can be used:

$$\phi(L,\tau) = \gamma S(\tau) - \frac{\sigma_{\mathrm{FCA}}\mu}{2} T(\tau), \tag{A6}$$

where $S(\tau) = \int_0^L P(z,\tau)dz$ and $T(\tau) = \int_0^L \bar{N}_c(z,\tau)dz$ need to be numerically calculated for the full range of TPA and FCA parameters expected and input powers used. We note that, when using the phase ansatz to fit the reconstructed phase profiles, only γ and μ are used as fit parameters: the in-waveguide power and TPA parameter are already deduced from the transmission measurements for each temperature setting.

A temperature-dependent model of FCA is used to model the expected transmission and output phase profiles. A suitable model for FCA is given by Refs. [46,47] as follows:

$$\sigma_{\mathrm{FCA}} = \frac{q_e^3\lambda^2}{4\pi^2\epsilon_0 c^3 n}\left(\frac{1}{m_e^{*2}\mu_e} + \frac{1}{m_h^{*2}\mu_h}\right), \tag{A7}$$

where q_e is the electron charge; ϵ_0 the permitivity of free space; c the speed of light; $n = 3.48$ the refractive index of silicon; $m_e^* = 0.3m_0$ and $m_h^* = 0.4m_0$ are the electron and hole effective masses expressed in terms of the free-electron mass, m_0; and μ_e and μ_h are the electron and hole mobilities. Although the carrier effective masses are in general temperature dependent, they are not expected to change significantly over the range of temperatures in our study [48]. Rather, the dominant contribution to the temperature dependence arises through the electron and hole mobilities. The empirical models for carrier mobility developed in Ref. [49] [see Eqs. (8) and (13) therein] show a temperature and density dependence of the carrier mobility. In our study, carrier densities are typically in the region of 10^{18} cm^{-3}, which results in a nearly constant mobility and, therefore, constant σ_{FCA}, from 300 K down to 50 K. Below 50 K, the carrier mobility is seen to increase rapidly, resulting in a rapid decrease in FCA as the temperature approaches 0 K.

Table I provide a selection of values for the nonlinear parameters used in our analysis as a function of temperature. The values for α_{TPA} and n_2 are those produced by the fitting functions (3) and (6) respectively, whereas σ_{FCA} values are from the FCA model (A7) and are used as an input to our numerical model.

APPENDIX B: CORRECTING FOR COUPLING ASYMMETRY

When measuring the fiber-to-fiber transmission though an on-chip waveguide in the linear-optical regime, it is impossible to independently determine the coupling losses. However, uncertainty in our knowledge of the on-chip power constitutes an important source of error when performing nonlinear measurements, as the measured nonlinear response varies quadratically with our estimate of the on-chip power. This error can lead to an incorrect estimate of the nonlinear parameters. However, by taking pairs of transmission measurements with light propagating in both directions, it is possible to determine the correct coefficients. We show this by considering only the TPA below, although this can be generalized in a straightforward way to include free-carrier effects as well. Consider the propagation equation (A4), where the only nonlinearity considered is TPA, as follows:

$$\frac{\partial P}{\partial z} = -\alpha_{\mathrm{TPA}}P^2 - \alpha P. \tag{B1}$$

We can introduce a rescaled power $p(z)$ such that $P(z,\tau) = P(0,\tau)p(z)$ and $p(0) = 1$ at the start of the waveguide. Then,

$$\frac{\partial p}{\partial z} = -Ap^2 - \alpha p, \tag{B2}$$

where $A = \alpha_{\mathrm{TPA}}P(0,\tau)$ and we write the solution as $p = p(z;A)$. By fitting this solution to our transmission data, the coefficient A can be found, although we note that individually α_{TPA} and $P(0,\tau)$ are still unknown. However, taking a pair of measurements in both orientations results in a pair of A coefficients, $A' = \alpha_{\mathrm{TPA}}P'(0)$ and $A'' = \alpha_{\mathrm{TPA}}P''(0)$, where the different powers at the start of the waveguide arise due to the asymmetric coupling losses. The waveguide has two grating couplers for coupling to external fibers, the losses of which we arbitrarily denote as η_L and η_R. We can therefore express the product of the A coefficients as

$$A'A'' = (\alpha_{\mathrm{TPA}}\eta_L P_{\mathrm{in}})(\alpha_{\mathrm{TPA}}\eta_R\sqrt{\eta_X}P_{\mathrm{in}}), \tag{B3}$$

where P_{in} is the power just before the input grating coupler and η_X is the total excess loss that is introduced by our cross-over switch when in the on state. However, when fitting each transmission power scan, we have no way of knowing η_L and η_R individually. Therefore, when fitting the transmission curve in each direction independently we *a priori* assume symmetric losses on both grating couplers as follows:

$$A'A'' = (\alpha'_{\mathrm{TPA}}\sqrt{\eta_L\eta_R}P_{\mathrm{in}})(\alpha''_{\mathrm{TPA}}\sqrt{\eta_L\eta_R\eta_X}P_{\mathrm{in}}), \tag{B4}$$

where α'_{TPA} and α''_{TPA} are the apparent TPA coefficients that we extract from each individual fitting and $\sqrt{\eta_L\eta_R}$ is the

average grating coupler loss. Comparing expressions (B3) and (B4), it is straightforward to show that the real TPA parameter can be calculated from the geometric mean of the apparent TPA parameters found from each individual fit as follows:

$$\alpha_{\mathrm{TPA}} = \sqrt{\alpha'_{\mathrm{TPA}}\alpha''_{\mathrm{TPA}}}. \tag{B5}$$

Thus, although we assume symmetric coupling when fitting the transmission curve in each direction, leading to unequal apparent TPA values, the correct TPA value can always be found by taking the geometric mean of these. This process can be generalized in a straightforward manner to include free-carrier effects, showing $\sigma_{\mathrm{FCA}} = \sqrt{\sigma'_{\mathrm{FCA}}\sigma''_{\mathrm{FCA}}}$. Similarly, by evaluating A'/A'', we find $\alpha'_{\mathrm{TPA}}/\alpha''_{\mathrm{TPA}} = \eta_L/\eta_R$, from which the individual coupling losses can be deduced as follows:

$$\eta_L^2 = \sqrt{\eta_L\eta_R}\left(\frac{\alpha'_{\mathrm{TPA}}}{\alpha''_{\mathrm{TPA}}}\right), \quad \eta_R^2 = \sqrt{\eta_L\eta_R}\left(\frac{\alpha''_{\mathrm{TPA}}}{\alpha'_{\mathrm{TPA}}}\right). \tag{B6}$$

[1] Austin G. Griffith, Ryan K. W. Lau, Jaime Cardenas, Yoshitomo Okawachi, Aseema Mohanty, Romy Fain, Yoon Ho Daniel Lee, Mengjie Yu, Christopher T. Phare, Carl B. Poitras, Alexander L. Gaeta, and Michal Lipson, Silicon-chip mid-infrared frequency comb generation, Nat. Commun. **6**, 6299 (2015).

[2] C. Lacava, M. J. Strain, P. Minzioni, I. Cristiani, and M. Sorel, Integrated nonlinear Mach Zehnder for 40 Gbit/s all-optical switching, Opt. Express **21**, 21587 (2013).

[3] F. Li, T. D. Vo, C. Husko, M. Pelusi, D.-X. Xu, A. Densmore, R. Ma, S. Janz, B. J. Eggleton, and D. J. Moss, All-optical XOR logic gate for 40 Gb/s DPSK signals via FWM in a silicon nanowire, Express **19**, 20364 (2011).

[4] Hiroshi Fukuda, Koji Yamada, Tetsufumi Shoji, Mitsutoshi Takahashi, Tai Tsuchizawa, Toshifumi Watanabe, Jun ichi Takahashi, and Sei ichi Itabashi, Four-wave mixing in silicon wire waveguides, Opt. Express **13**, 4629 (2005).

[5] Mark A. Foster, Amy C. Turner, Jay E. Sharping, Bradley S. Schmidt, Michal Lipson, and Alexander L. Gaeta, Broad-band optical parametric gain on a silicon photonic chip, Nature **441**, 960 (2006).

[6] Jay E. Sharping, Kim Fook Lee, Mark A. Foster, Amy C. Turner, Bradley S. Schmidt, Michal Lipson, Alexander L. Gaeta, and Prem Kumar, Generation of correlated photons in nanoscale silicon waveguides, Opt. Express **14**, 12388 (2006).

[7] Imad I. Faruque, Gary F. Sinclair, Damien Bonneau, John G. Rarity, and Mark G. Thompson, On-chip quantum interference with heralded photons from two independent micro-ring resonator sources in silicon photonics, Opt. Express **26**, 20379 (2018).

[8] Qianfan Xu and Michal Lipson, All-optical logic based on silicon micro-ring resonators, Opt. Express **15**, 924 (2007).

[9] T. Kampfrath, D. M. Beggs, T. P. White, A. Melloni, T. F. Krauss, and L. Kuipers, Ultrafast adiabatic manipulation of slow light in a photonic crystal, Phys. Rev. A **81**, 043837 (2010).

[10] Alan D. Bristow, Nir Rotenberg, and Henry M. van Driel, Two-photon absorption and kerr coefficients of silicon for 850–2200 nm, Appl. Phys. Lett. **90**, 191104 (2007).

[11] Q. Lin, J. Zhang, G. Piredda, R. W. Boyd, P. M. Fauchet, and G. P. Agrawal, Dispersion of silicon nonlinearities in the near infrared region, Appl. Phys. Lett. **91**, 021111 (2007).

[12] H. K. Tsang and Y. Liu, Nonlinear optical properties of silicon waveguides, Semicond. Sci. Technol. **23**, 064007 (2008).

[13] M. Dinu, Dispersion of phonon-assisted nonresonant third-order nonlinearities, IEEE J. Quantum Electron. **39**, 1498 (2003).

[14] Hernando Garcia and Ramki Kalyanaraman, Phonon-assisted two-photon absorption in the presence of a dc-field: The nonlinear Franz–Keldysh effect in indirect gap semiconductors, J. Phys. B: At. Mol. Opt. Phys. **39**, 2737 (2006).

[15] J. L. Cheng, J. Rioux, and J. E. Sipe, Full band structure calculation of two-photon indirect absorption in bulk silicon, Appl. Phys. Lett. **98**, 131101 (2011).

[16] John F. Reintjes and James C. McGroddy, Indirect Two-Photon Transitions in Si at 1.06 μm, Phys. Rev. Lett. **30**, 901 (1973).

[17] K. G. Svantesson and N. G. Nilsson, Determination of the temperature dependence of the free carrier and interband absorption in silicon at 1.06 μm, J. Phys. C: Solid State Phys. **12**, 3837 (1979).

[18] Wolfram H. P. Pernice, Carsten Schuck, Mo Li, and Hong X. Tang, Carrier and thermal dynamics of silicon photonic resonators at cryogenic temperatures, Opt. Express **19**, 3290 (2011).

[19] Terry Rudolph, Why I am optimistic about the silicon-photonic route to quantum computing, APL Photonics **2**, 030901 (2017).

[20] J. P. Sprengers, A. Gaggero, D. Sahin, S. Jahanmirinejad, G. Frucci, F. Mattioli, R. Leoni, J. Beetz, M. Lermer, M. Kamp, S. Höfling, R. Sanjines, and A. Fiore, Waveguide superconducting single-photon detectors for integrated quantum photonic circuits, Appl. Phys. Lett. **99**, 181110 (2011).

[21] W. H. P. Pernice, C. Schuck, O. Minaeva, M. Li, G. N. Goltsman, A. V. Sergienko, and H. X. Tang, High-speed and high-efficiency travelling wave single-photon detectors embedded in nanophotonic circuits, Nat. Commun. **3**, 1325 (2012).

[22] Gary F. Sinclair and Mark G. Thompson, Effect of self- and cross-phase modulation on photon pairs generated by spontaneous four-wave mixing in integrated optical waveguides, Phys. Rev. A **94**, 063855 (2016).

[23] Chad A. Husko, Alex S. Clark, Matthew J. Collins, Alfredo De Rossi, Sylvain Combrié, Gaëlle Lehoucq, Isabella H. Rey, Thomas F. Krauss, Chunle Xiong, and Benjamin J. Eggleton, Multi-photon absorption limits to heralded single photon sources, Sci. Rep. **3**, 3087 (2013).

[24] Ricardo Claps, Dimitri Dimitropoulos, Yan Han, and Bahram Jalali, Observation of Raman emission in silicon waveguides at 1.54 μm, Opt. Express **10**, 1305 (2002).

[25] Stéphane Clemmen, Antony Perret, Jassem Safioui, Wim Bogaerts, Roel Baets, Simon-Pierre Gorza, Philippe Emplit, and Serge Massar, Low-power inelastic light scattering at small detunings in silicon wire waveguides at telecom wavelengths, J. Opt. Soc. Am. B **29**, 1977 (2012).

[26] Richard Soref, Mid-infrared photonics in silicon and germanium, Nat. Photonics **4**, 495 (2010).

[27] Yi Zou, Swapnajit Chakravarty, Chi-Jui Chung, Xiaochuan Xu, and Ray T. Chen, Mid-infrared silicon photonic waveguides and devices, Photon. Res. **6**, 254 (2018).

[28] Ajanta Barh, Peter Tidemand-Lichtenberg, and Christian Pedersen, Thermal noise in mid-infrared broadband upconversion detectors, Opt. Express **26**, 3249 (2018).

[29] Lianghong Yin and Govind P. Agrawal, Impact of two-photon absorption on self-phase modulation in silicon waveguides, Opt. Lett. **32**, 2031 (2007).

[30] I. D. Rukhlenko, M. Premaratne, C. Dissanayake, and G. P. Agrawal, Nonlinear pulse evolution in silicon waveguides: An approximate analytic approach, J. Lightwave Technol. **27**, 3241 (2009).

[31] Govind P. Agrawal, *Nonlinearfiber Optics* (Academic Press, San Diego, 2001, 3rd ed).

[32] K. G. Svantesson, Determination of the interband and the free carrier absorption constants in silicon at high-level photoinjection, J. Phys. D: Appl. Phys. **12**, 425 (1979).

[33] M. D. Thomson, J. M. Dudley, L. P. Barry, and J. D. Harvey, Complete pulse characterization at 1.5 μm by cross-phase modulation in optical fibers, Opt. Lett. **23**, 1582 (1998).

[34] Tom Baehr-Jones, Ran Ding, Ali Ayazi, Thierry Pinguet, Matt Streshinsky, Nick Harris, Jing Li, Li He, Mike Gould, Yi Zhang, Andy Eu-Jin Lim, Tsung-Yang Liow, Selin Hwee-Gee Teo, Guo-Qiang Lo, and Michael Hochberg, A 25 Gb/s silicon photonics platform, arXiv:1203.0767 (2012).

[35] G. F. Sinclair, N. A. Tyler, D. Sahin, J. Barreto, and M. G. Thompson, Data for: "Temperature dependence of the Kerr nonlinearity and two-photon absorption in a silicon waveguide at 1.55 μm," https://doi.org/10.5523/bris.1ii7ungb46zb22kcclh2kj99ja (2019).

[36] K. Bücher, J. Bruns, and H. G. Wagemann, Absorption coefficient of silicon: An assessment of measurements and the simulation of temperature variation, J. Appl. Phys. **75**, 1127 (1994).

[37] Y. P. Varshni, Temperature dependence of the energy gap in semiconductors, Physica **34**, 149 (1967).

[38] P. K. Basu, *Theory of Optical Processes in Semiconductors* (Oxford University Press, New York, 1997).

[39] J. R. Fienup, Phase retrieval algorithms: A comparison, Appl. Opt. **21**, 2758 (1982).

[40] Victor Mizrahi, K. W. DeLong, G. I. Stegeman, M. A. Saifi, and M. J. Andrejco, Two-photon absorption as a limitation to all-optical switching, Opt. Lett. **14**, 1140 (1989).

[41] Qiang Lin, J. Zhang, Giovanni Piredda, Robert W. Boyd, Philippe M. Fauchet, and Govind P. Agrawal, Dispersion of silicon nonlinearities in the near infrared region, Appl. Phys. Lett. **91**, 21111 (2007).

[42] D. N. Klyshko, Utilization of vacuum fluctuations as an optical brightness standard, Soviet J. Quantum Electron. **7**, 591 (1977).

[43] J. G. Rarity, K. D. Ridley, and P. R. Tapster, Absolute measurement of detector quantum efficiency using parametric downconversion, Appl. Opt. **26**, 4616 (1987).

[44] G. G. Macfarlane, T. P. McLean, J. E. Quarrington, and V. Roberts, Fine structurein the absorption-edge spectrum of Si, Phys. Rev. **111**, 1245 (1958).

[45] Q. Lin, Oskar J. Painter, and Govind P. Agrawal, Nonlinear optical phenomena in silicon waveguides: Modeling and applications, Opt. Express **15**, 16604 (2007).

[46] D. K. Schroder, R. N. Thomas, and J. C. Swartz, Free carrier absorption in silicon, IEEE J. Solid State Circuits **13**, 180 (1978).

[47] Xiankai Sun, Xufeng Zhang, Carsten Schuck, and Hong X. Tang, Nonlinear optical effects of ultrahigh-Q silicon photonic nanocavities immersed in superfluid helium, Sci. Rep. **3**, 1436 (2013).

[48] D. M. Riffe, Temperature dependence of silicon carrier effective masses with application to femtosecond reflectivity measurements, J. Opt. Soc. Am. B **19**, 1092 (2002).

[49] N. D. Arora, J. R. Hauser, and D. J. Roulston, Electron and hole mobilities in silicon as a function of concentration and temperature, IEEE Trans. Electron Devices **29**, 292 (1982).